Modeling of relative permeabilities including dynamic wettability transition zones

Abay Molla Kassa [a,b,*], Sarah E. Gasda [a], Kundan Kumar [b], Florin A. Radu [b]

[a] *NORCE Norwegian Research Center, Bergen, Norway*
[b] *Department of Mathematics, University of Bergen, Norway*

ARTICLE INFO

ABSTRACT

Wettability is a pore-scale property that impacts the relative movement and distribution of fluids in a porous medium. There are reservoir fluids that provoke the surface within pores to undergo a wettability change. This wettability change, in turn, alters the dynamics of relative permeabilities at the Darcy scale. Thus, modeling the impact of wettability change in the relative permeabilities is essential to understand fluids interaction in porous media. In this study, we include time-dependent wettability change into the relative permeability–saturation relation by modifying the existing relative permeability function. To do so, we assume the wettability change is represented by the sorption-based model that is exposure time and chemistry dependent. This pore-scale model is then coupled with a triangular bundle-of-tubes model to simulate exposure time-dependent relative permeabilities data. The simulated data is used to characterize and quantify the wettability dynamics in the relative permeability–saturation curves. This study further shows the importance of accurate prediction of the relative permeability in a dynamically altering porous medium.

1. Introduction

Wettability alteration (WA) plays an important role in many industrial applications such as microfluidics nanoprinting, enhanced oil recovery (EOR), and CO_2 storage (Bonn et al., 2009; Iglauer et al., 2014, 2016; Yu et al., 2008; Blunt, 2001). Wettability refers to the tendency of one fluid over the others to spread on or adhere to a solid surface (Falode and Manuel, 2014; Bonn et al., 2009) and is defined by the fluid-fluid contact angle (CA). This pore-scale property regulates the distribution of fluids in the pore spaces and controls the relative flow of immiscible fluids in a porous medium (Anderson, 1987; Bobek et al., 1958; Falode and Manuel, 2014; Bonn et al., 2009). This, in turn, impacts constitutive relations in the multi-phase flow systems such as residual saturation, relative permeability, and capillary pressure at the Darcy scale (Ahmed and Patzek, 2003; Pentland et al., 2011; Iglauer et al., 2011, 2014; Falode and Manuel, 2014). Investigating and upscaling the impact of WA on the constitutive relations is of great importance.

Wettability is assumed to be static in time and uniform in space. However, wettability can be a dynamic process that depends on surface chemistry, composition of fluids, exposure time, and reservoir conditions (pressure and temperature) to name a few (Du et al., 2019;

Salathiel, 1973; Treiber et al., 1972; Anderson, 1987; Haagh et al., 2017; Jadhunandan and Morrow, 1995; Buckley et al., 1988; Morrow, 1970). Experiments on crude oil/brine/rock systems have shown that adsorption of active components from the crude oil is able to change the wettability of the sample porous medium from water-wet to intermediate-wet system, a process known as ageing (Salathiel, 1973; Anderson, 1986; Buckley et al., 1988). It is also hypothesized that the oil reservoir may be more oil-wet than what is observed from the experiment. This is because the adsorption time of the experiment period was much less than the age of the oil in the reservoir. Furthermore, CO_2 s one of the reservoir fluids which contain active components that can provoke the surface within the pores to undergo a WA (Wang et al., 2013; Bikkina, 2011; Yang et al., 2008; Dickson et al., 2006; Iglauer et al., 2012, 2014; Jung and Wan, 2012; Espinoza and Santamarina, 2010; Farokhpoor et al., 2013; Saraji et al., 2013).

Generally, the WA process can have three phases that delineate the transition from initial to final wetting-state conditions, e.g. initial-wet, final-wet, and dynamic-wet. The end (initial and final) wetting conditions are static in time but can be uniform and/or mixed in space. A mixed-wet condition could be created by rock mineral and exposure history differences. This is due to the fact that a pore surface exposed to

the WA agent may be altered to a new wetting condition, while the unexposed surface keeps the initial wetting state (Kovscek et al., 1993; Blunt, 1997). This creates a mixed-wet condition even within a single pore and was observed and explained first by Salathiel et al. (Salathiel, 1973) in the 1970s. Often, WA is assumed to occur instantaneously and is considered as a function of the WA agent concentration. In some cases, however, the alteration process might take prolonged time in the scale of weeks and months (Tokunaga and Jiamin, 2013; Wang and Tokunaga, 2015; Buckley et al., 1988; Powers et al., 1996). Non-instantaneous WA, or aging, occurs when surface processes such as adsorption or chemical alteration are gradual rather than spontaneous. In this regard, the dynamic-wet phase can be a function of exposure time in addition to the WA agent concentration.

The WA process may result in a saturation function alteration for subsequent drainage-imbibition displacements and thus cause hysteresis in constitutive relations (Vives et al., 1999; Ahmed and Patzek, 2003; Delshad et al., 2003; Spiteri et al., 2008; Landry et al., 2014). For instance, core-flooding measurements for (supercritical or gas) CO_2-water system have shown that WA-induced alteration in the residual saturation and capillary pressure curves occurs despite the fact that they were measured following a standard procedure, i.e., where "pressure equilibration" is obtained after each increment in pressure (Plug and Bruining, 2007; Wang et al., 2013, 2016; Tokunaga and Jiamin, 2013; Tokunaga et al., 2013; Kim et al., 2012). In these measurements, a steadily change in capillary pressure function over time was observed. More importantly, the capillary pressure deviation from the initial-wet state curve could not be explained by classical scaling arguments. The instability and gradual change of residual saturation and capillarity through exposure time, in turn, impact the behavior of relative permeabilities.

The above experiments reveal that more complex constitutive functions are required to correlate the relative permeability and capillary pressure data that are impacted by WA. One alternative is to use mixed-wet model, e.g. Kjosavik et al. (2002) and Lomeland et al. (2005), that capture the static heterogeneity of wettability in the relative permeabilities. The main feature of these models is their flexibility to describe hysteresis and scanning curves caused by a wettability gradient in space. Other alternatives are models designed to handle the instantaneous WA process in the relative permeabilities. The first class of these models involves a heuristic approach that interpolates between the initial and final wetting states in which the WA effect is captured as a coefficient function (Delshad et al., 2009; Yu et al., 2008; Anderson et al., 2015; Adibhatia et al., 2005; Sedaghat and Azizmohammadi, 2019). Interpolation models are conceptually simple, while the initial and final wetting states are characterized by standard functions, e.g. Brooks-Corey (Brooks and Corey, 1964) or van Genuchten (van Genuchten, 1980)). The other approach incorporates the effect of the instantaneous WA into the relative permeabilities through the residual saturation directly (Lashgari et al., 2016). To date, only Al-Mutairi et al. (2012) have considered the effect of time-dependent WA in both the relative permeabilities and capillary pressure functions explicitly. The authors include a time-dependent mechanism for CA change within the residual saturation, which in turn affects the relative permeability and capillary pressure functions through the effective saturation. However, their model does not sufficiently incorporate or upscale the WA processes to core-scale laws.

Appropriate upscaling of the pore-scale time-dependent WA process connected to the capillary pressure function was the subject of our recent work (Kassa et al., 2020). There, WA dynamics were upscaled by introducing a mechanistic time-dependent CA model at the pore-level that was coupled with a cylindrical bundle-of-tubes model and used to simulate capillary pressure curves for drainage and imbibition displacements. The simulated data was used to formulate and quantify an interpolation-based capillary pressure model at the Darcy scale. The new dynamic model resolves the existing interpolation models used in the studies of reservoir simulation (Adibhatia et al., 2005; Delshad et al.,

2009; Yu et al., 2008; Anderson et al., 2015; Sedaghat and Azizmohammadi, 2019) by including the dynamics in time and quantifying the pore-scale WA process to the interpolation model in a systematic manner.

One may consider employing a similar approach to (Kassa et al., 2020) and an interpolation-type model to capture the pore-scale underpinnings of WA in the relative permeability behaviors. However, time-dependent WA may impact the capillary pressure and relative permeabilities in different ways. As observed in Kassa et al. (2020), WA has a direct impact on the entry pressure in each pore and reflects it at the Darcy scale. Furthermore, a small change in CA exerts a large impact on the dynamics of the capillary pressure function. However, the relative permeability alteration occurs when the WA affects the pore filling/draining orders of pore sizes. This may lead to a longer exposure time to observe a relative permeability deviation from the initial-wet state curve. Furthermore, unlike the capillary pressure function, the relative permeability curves are constrained between zero and one for any change of wettability. These features of the relative permeability may impact the modeling approach to upscale the pore-scale WA processes to core scale.

To our knowledge, a physically reliable model to characterize a prolonged exposure time-dependent WA induced dynamics in the relative permeability behaviors has not been proposed yet. This paper modifies and extends the approach discussed in Kassa et al. (2020) to develop a reliable model for dynamic relative permeability that accounts for pore-level time-dependent WA processes. In Section 2, we present the upscaling workflow based on simulation of dynamic relative permeability data using a pore-scale model for displacement coupled with CA change. Section 3 describes the correlation of two possible dynamic relative permeability models with associated analysis.

2. Modeling, simulation, and upscaling approach

A time-dependent WA may introduce a dynamics in the relative permeability–saturation ($k_{r\alpha} - S_\alpha$) relationship. The dynamics can be measured by its deviation from the static initial wetting-state as:

$$k_{r\alpha}(\cdot) - k_{r\alpha}^{in}(S_\alpha) := f_\alpha^{dyn}(\cdot), \tag{1}$$

where f_α^{dyn} represents the dynamic component. Alternatively, parameters of the standard models can be correlated with the dynamics,

$$k_{r\alpha}(\cdot) = k_{r\alpha}^{i}(S_\alpha, p_1(\cdot), p_2(\cdot), \ldots), \tag{2}$$

where $p_{i=1,2,\ldots,n}(\cdot)$ represent n fitting parameters that change along exposure time. In the above equations, the subscript $\alpha \in \{w, n\}$ represents the wetting and non-wetting phases, respectively. In this study, we explore both dynamic approaches in Eqs. (1) and (2) to quantify and characterize dynamics in relative permeability for a system that undergoes WA.

From the first approach, Eq. (1), we propose an *interpolation-based* model following our previous work (Kassa et al., 2020), where the dynamic component is designed to interpolate between two end wetting-state curves. To obtain an interpolation model, f_α^{dyn} can be scaled by the difference between the initial and final wetting-state relative permeability curves. The resulting non-dimensional quantity is:

$$\omega_\alpha(k_{r\alpha}^f - k_{r\alpha}^{in}) = f_\alpha^{dyn}, \tag{3}$$

where ω is referred to as the *dynamic coefficient*, and superscript *in* and *f* represents relative permeabilities at the initial and final wettingstates, respectively. This can be substituted into Eq. (1) to obtain an interpolation model for dynamic relative permeability:

$$k_{r\alpha} = (1 - \omega_\alpha)k_{r\alpha}^{in} + \omega_\alpha k_{r\alpha}^f, \tag{4}$$

where ω_α is then correlated to wettability dynamics at the macroscale.

Similar models to Eq. (4) were employed to include the impact of instantaneous WA on relative permeability (Delshad et al., 2009; Yu et al., 2008; Anderson et al., 2015; Adibhatia et al., 2005; Sedaghat and Azizmohammadi, 2019).

The second approach (Eq. (2)) is a *parameter-based* approach that relies on a systematic inclusion of the dynamic term f_α^{dyn} into the relative permeability function through the model parameters. This can be done by formulating the parameters $p_i(\cdot)$ as a function of exposure time and WA agent in similar fashion as ω_α. This approach is motivated by the fact that the parameters in the standard relative permeability models are adjusted to different values when wettability changes from one state to the other.

Both the initial and final wetting-state curves can be characterized fully by the well-known relative permeability models such as van Genuchten (van Genuchten, 1980) or Brooks-Corey (Brooks and Corey, 1964), Purcell (Li and Horne, 2006), the LET model (Lomeland et al., 2005) or a model proposed by Kjosavik et al. (2002). For the sake of brevity, we focus on the Brooks-Corey (BC) and LET models in this study. The BC relative permeabilities can be derived by integrating the capillary pressure over the capillary tubes (Xu et al., 2016; Kjosavik et al., 2002). After the integration of the BC capillary pressure, one can obtain relative permeabilities:

$$k_{rw}^{in} = S_w^{a_w}, \text{and} \quad k_{rn}^{in} = \left(1 - S_w^{a_w}\right)\left(1 - S_w\right)^{m_n}, \tag{5}$$

for the water-wet system and,

$$k_{rw}^f = \left(1 - S_w^{a_w}\right)\left(1 - S_n\right)^{m_w}, \text{and} \quad k_{rn}^f = S_n^{a_n}, \tag{6}$$

for a hydrophobic system (see (Kjosavik et al., 2002)), here a_α and m_α are phase-specific parameters that can be utilized as dynamic fitting parameters $p_{i=1,2}$ in Eq. (2). Particularly, m_α is known as the tortuosity exponent.

In 2005, Lomeland et al. (2005) have proposed relative permeability models to predict the relative permeability curves for any type of wettability conditions:

$$k_{rw}^{in} = \frac{S_w^{L_w}}{S_w^{L_w} + E_w(1 - S_w)^{T_w}}, \text{and} \quad k_{rn}^{in} = \frac{(1 - S_w)^{L_n}}{(1 - S_w)^{L_n} + E_n S_w^{T_n}}, \tag{7}$$

where L_α, E_α, and T_α are empirical parameters for each phase. A detailed description and explanation of the parameters can be found in Lomeland et al. (2005). In this study, the LET parameters can be utilized as dynamic fitting parameters, $p_{i=1,2,...,6}$ in Eq. (2).

2.1. Overall upscaling workflow

The two approaches described above are the basis for correlating WA-induced dynamics in relative permeability data. The first step in this workflow is generating relative permeability data by flow experiments under static flow conditions, i.e. a fixed pressure gradient and saturation. Once steady-state is reached, the relative permeability can be inferred from Darcy's Law for multi-phase flow:

$$k_{r\alpha}(S_\alpha) = \frac{Q_\alpha \mu_\alpha L}{K A_T \Delta P_\alpha}, \tag{8}$$

where S_α is the average saturation of phase α, Q_α is the volumetric flow rate, K is the absolute permeability, and A_T is the cross-sectional area of the domain.

Laboratory experiments can be performed to generate $k_{r\alpha}$-S_α data, however this approach is expensive and time-consuming. Existing laboratory data are currently unavailable for systems that undergo long-term WA. Thus, we follow a theoretical approach in which we simulate time-dependent $k_{r\alpha}$-S_α data from a pore-scale model. The pore-scale experiments are performed in a similar fashion to laboratory experiments. A given pressure drop will induce flow through pores where the

entry pressure is exceeded, which is a function of pore geometry and wetting state. Once static flow is reached, relative permeability is calculated according to Eq. (8) as a function of the average saturation, which can be computed by volume averaging over the pore-scale domain.

An important step in switching from laboratory to numerical experiments is explicitly accounting for WA in each individual pore. We model WA through a change in CA from an initial to final wetting state as a function of exposure time to the WA agent, in our case the non-wetting fluid phase. Exposure time in our study is associated with the time to reach steady state for each data point in $k_{r\alpha}$-S_α space. This time component is driven by the displacement mechanisms occurring at the pore scale. For each new data point, time accumulates, WA progresses, and relative permeability is altered continuously throughout the experiment. The experiment continues along several drainage-imbibition cycles until WA is complete and the end wetting state is reached. The result is a complete set of $k_{r\alpha}$-S_α data and associated WA dynamics.

The next step is to perform correlations for both the interpolation-based and parameter-based dynamic models in Eqs. (1) and (2) respectively. This procedure involves traditional curve-fitting, but we also apply insight about wettability dynamics and detailed analysis to arrive at a suitable and easy-to-implement dynamic model for reservoir simulation. We test each model for its suitability in capturing relative permeability dynamics. The goal is to develop a correlated model that involves only a few parameters.

After arriving at a suitable dynamic model correlation to the simulated data, we extend our analysis to ensure the robustness of the fitted model to a generic path in saturation-time domain. And finally, we examine the relation between the fitting parameter(s) of the upscaled relative permeability model and the parameter controlling CA change at the pore scale. This final step is important for linking the form of the macroscale model to pore-scale processes.

2.2. Pore-scale model description

We employ a triangular bundle-of-tubes to represent the pore-scale in quantifying the upscaled relative permeability given in Eq. (8). This representation of the pore scale was chosen to utilize the simplicity of a bundle-of-tubes model but with additional complexity to capture different fluid distributions and mixed wetting conditions within a single pore. Triangular tubes can support corner fluids and drainage through layers (Kovscek et al., 1993; Hui and Blunt, 2000; Helland and Skjæveland, 2006b).

A bundle-of-tubes model is a collection of capillary tubes with a distribution of radii as depicted in Fig. 1. The tubes in Fig. 1 are connected with the wetting (right with pressure P_r^{res}) and non-wetting (left with pressure P_l^{res}) phase reservoirs. Once the fluid movement is initiated in the tubes, the fluid configurations in each tube can have the form as in Fig. 1. Here, $A_{b,m}$ and $A_{c,m}$ are bulk and corner areas, respectively, that cover the cross-section of a tube and sum to be the area of the triangle (Fig. 1c). The quantity dx represents the change of interface location along the tube, whereas α_m is the half angle and θ_m is the fluid-fluid CA. Here, θ_m is the bulk surface CA in a given tube that represents the CA for an advancing or receding front during drainage or imbibition, where the angle may be hysteretic. θ_m also becomes the hinging angle $\theta_{h,m}$ if the interface hinges in the corner of the tube after displacement is completed. Detailed calculations of the areas and angles are discussed in the Apprndix A.

Let the boundary pressures difference be defined as:

$$\Delta P = P_l^{res} - P_r^{res}, \tag{9}$$

and the tubes in the bundle are filled with the wetting phase initially. Each tube has an entry pressure $P_{c,m}$ associated with it. If $\Delta P > P_{cap,m}$ is satisfied, the non-wetting fluid starts to displace the wetting phase, and
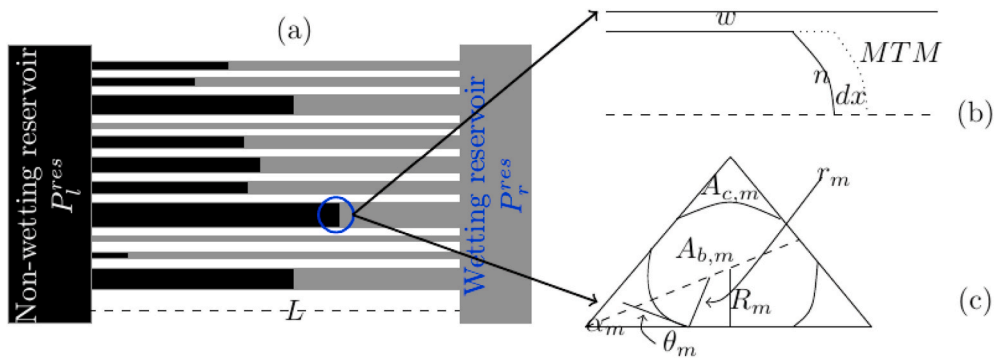
Fig. 1. The fluid displacement scenario in a bundle of tubes that is connected with wetting and non-wetting phase reservoirs. The right column shows fluid distribution during primary drainage: (b) shows the side-view and (c) shows the front view of the cross-section. The MTM refers to the main terminal meniscus. For complete (drainage-imbibition cycles) fluid configurations, see Fig. 2.
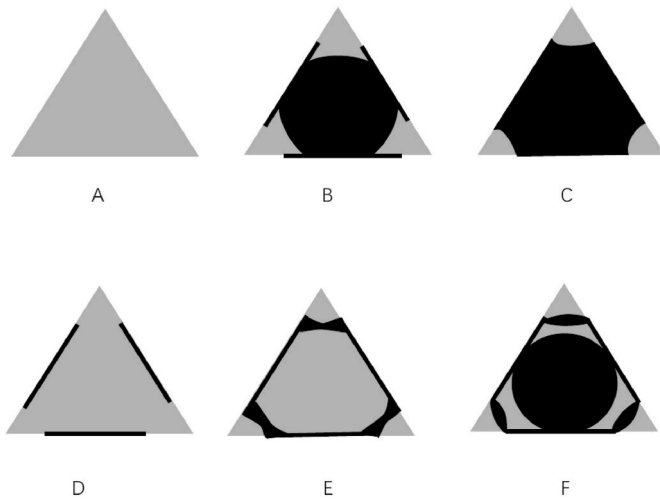

Fig. 2. Fluid configurations for initial condition (A), primary drainage (B or C), imbibition (D or E), and secondary drainage (F). Wetting phase is given in a light color and non-wetting phase in a dark color. We adopted the configurations from Helland and Skjæveland (2006b). The bold lines along the sides indicate altered wettability.

the volumetric flow rate in tube m can be approximated by the Lucas-Washburn flow model (Washburn, 1921):

$$q_m = \frac{\mathscr{G}_m(R_m, \theta_m)\left[\Delta P - P_{cap,m}\right]}{8\left[\mu_n x_m^{int} + \mu_w\left(L - x_m^{int}\right)\right]}, \tag{10}$$

where, μ_α is the phase viscosity, x_m^{int} is the location of the fluid-fluid interface along the length L of tube m, where $q_m = dx_m^{int}/dt$ is the interface velocity.

The quantity $\mathscr{G}_m$ in Eq. (10) represents the conductance of the fluids within tube m. We follow the work of Hui and Blunt (2000) to pre-compute the conductance. Conductance of tube m is a function of tube geometry, given by the inscribed radius R_m, the contact angle at the front, given by θ_m, and the configuration of fluids in the tube, which is itself dependent on wettability and filling history as described below.

The wettability change or gradient in triangular pores may create distinct fluid configurations after subsequent drainage and imbibition displacements (see Fig. 2). We summarize in brief the range of possible fluid configurations, and the reader is referred to Helland et al. (Helland and Skjæveland, 2006a) for the details of the fluid configurations. Configuration A shows a pore that is filled with the wetting phase and the wettability is representing the initial (water-wet) wetting state. A drainage into configuration A would result in either configuration B or C

depending on the wettability. Subsequent imbibition into configuration B would always give configuration D, whereas imbibition into configuration C may result in either configuration D or E. Configuration F may occur after a drainage process that starts from configuration E if the receding CA is sufficiently smaller than the previous advancing CA. Otherwise, a drainage into configuration E would give configuration B or C.

The capillary pressure in Eq. (10) is given by

$$P_{cap,m} = \frac{\sigma}{r_m}, \tag{11}$$

where r_m is radius of arc meniscus (AMs) that separates the bulk from the corner fluid, and σ is fluid-fluid interfacial tension. The radius of curvature r_m is determined from the minimization of Helmholtz free energy of the system (Helland and Skjæveland, 2007). For isothermal, constant total volume, constant chemical potentials, and incompressible system, the minimization of the change in Helmholtz free energy can be simplified to (Helland and Skjæveland, 2007; Morrow, 1970; Bradford and Leij, 1997):

$$P_{cap,m}dV_n = \sigma(dA_{nw} + \cos(\theta_m)dA_{ns}), \tag{12}$$

where dV_n is the change of non-wetting fluid volume, dA_{nw} and dA_{ns} represent the change in interfacial area of fluid-fluid and fluid-solid interfaces, respectively (Helland and Skjæveland, 2007). A_{nw} and A_{ns} are longitudinal interfacial areas, distinct from the cross-sectional areas $A_{b,m}$ and $A_{c,m}$ depicted in Fig. 1.

Following (Helland and Skjæveland, 2006b; van Dijke and Sorbie, 2006; Ma et al., 1996), we calculate the entry pressure curvature, r_m, by combining Eqs. (11) and (12) for the starting configuration prior to drainage or imbibition, i.e. one of the configurations depicted in Fig. 2. Then, after a displacement occurs, the new fluid distribution is computed. This calculation involves determining the fluid volumes in the bulk ($A_{b,m}L$) and corners ($A_{c,m}L$) as a function r_m and θ_m. For mixed wetting conditions in tube m, θ_m affects the fluid configuration and thus determines the hinging CA, $\theta_{h,m}$. The hinging CA, $\theta_{h,m}$, is created after the MTM displaces the resident fluid and it evolves according to the change in θ_m. Furthermore, the areas ($A_{b,m}$ and $A_{c,m}$) are also pressure drop dependent in addition to wettability (θ_m). For example, the wetting phase in the corner area bulges out (configuration C) and starts moving (Configuration B) as (the pressure drop decreases) during the imbibition process occurring in other tubes. These calculations are based on different conditions such as the existence of the corner fluids, the fluid displacement history, the value of θ_m compared to the half angle (α_m), and similar geometrical or flow arguments. We refer the reader to the Appendix A for more details on these calculations.

2.3. Pore-scale wettability alteration

Above, we observed that the entry pressure in Eq. (12), fluid distributions in Appendix A, and conductance (Hui and Blunt, 2000) are wettability evolution dependent. In this section, we propose a model for CA change in tube m as a function of exposure time and fluid-history, based on the following assumptions:

- The CA of the pore surface is altered through exposure time to the WA agent and the alteration is permanent and cannot be restored to the original wetting condition when the WA agent is removed from the pore.
- WA is quasi-static in time if the WA agent is removed from the pore before the final wetting-state is reached. If the agent is reintroduced at some later point, alteration continues until the final state.

According to the assumptions above, only the bulk area of the tube covered by the non-wetting fluid during drainage (i.e. $A_{b,m}$) is altered dynamically in time, whereas the undrained corner surface area, defined by $A_{c,m} > 0$, remains at the initial condition. This may create a mixed-wet condition within a single tube. As we recall, wettability only impacts fluid configuration and displacement through the bulk CA θ_m. Thus, we can introduce a functional form to describe the CA change for θ_m as follows:

$$\theta_m(\cdot) := \theta_m^{in} + \varphi_m(\cdot)\left(\theta_m^f - \theta_m^{in}\right), \tag{13}$$

where θ_m^f, θ_m^{in} are the final and initial contact angles respectively. The WA model (13) is designed to evolve from an arbitrary initial wetting state to the final wetting condition so that φ_m is used to interpolate between end wetting conditions and has a value between zero and one.

Theoretical investigation and detailed laboratory measurement on time-dependent WA are very limited. Furthermore, WA is a complex process, where surface free energies, surface mineralogy, fluid composition and exposure time interact. However, adsorption of the WA agent onto the surface area is a natural process in CA change (Blunt, 2017). Such adsorption type wettability evolution is observed for CA measurements (Dickson et al., 2006; Jung and Wan, 2012; Iglauer et al., 2012; Jafari and Jung, 2016; Davis et al., 2003; Morton et al., 2005). These all give an insight to model φ in Eq. (13) according to the adsorption of the WA agent and can be given as follows:

$$\varphi_m := \frac{\chi_m}{C + \chi_m}, \tag{14}$$

where C is a non-dimensional parameter (it can be seen as the ratio of the adsorption and desorption rate constants) that controls the speed and extent of alteration from initial-wet to final-wet system. The derivation of Eq. (14) can be found in our previous work (Kassa et al., 2020). The variable χ_m is a measure of exposure time and is defined as:

$$\chi_m := \frac{1}{\mathcal{T}} \int_0^t \frac{A_{b,m} x_m^{int}(\tau)}{V_{p,m}} d\tau, \tag{15}$$

where $V_{p,m}$ is the pore volume of tube m, and $\mathcal{T}$ is a macroscale characteristic time that used to scale the exposure history. Without losses of generality, the characteristic time $\mathcal{T}$ is identical for all tubes and is pre-computed from Eq. (10) as the time for one complete drainage-imbibition cycle for the entire bundle of tubes under static initial wetting conditions.

The interface position x_m^{int} varies from 0 to L as determined by Eq. (10). We note the time interval used in Eq. (15) is the same for every tube, i.e. from the start of the relative permeability experiment until the current time. This implies that the integrand in Eq. (15) will be 0 or 1 for tube m during most of the experiment, since the local time for the interface to traverse the tube length is minimal compared to the total length of the experiment. This is because the pressure increments are set

to drain/imbibe one tube at a time.

The dependency of exposure time on local interface displacement results in a different χ_m for different tubes. This variation in χ gives rise to a *non-uniform* wetting condition across the bundle that persists until all pores have reached the final wetting-state. Heterogeneity in CA from tube to tube is distinct from mixed-wet conditions at the tube-level that evolves from application of Eq. (13). In this study, we do not consider the further complication of a wettability gradient across the length of the tubes because the time to drain is assumed to be fast compared to the exposure time for WA to occur.

2.4. Simulation approach

The pore-scale wettability dynamics described in Eqs. (13)–(15) are coupled to the pore-scale model formulation in Section 2.2 through alteration of θ_m. A series of drainage and imbibition cycles are then performed to generate the data needed to calculate relative permeability for each phase α according to Eq. (8). The included algorithm describes the steps taken in each cycle.

Algorithm: A single drainage-imbibition cycle for simulation of relative permeability data.

Drainage displacement: Set the maximum entry pressure, P_{cap}^{max}

    Calculate $P_{cap,m}$ from Eqs. (11)-(12) for each tube m
    if $\Delta P > P_{cap,m}$ **then**
        Drain the respective tubes until static flow conditions are reached
        Estimate t from Eq. (10) and χ_m from Eq. (15)
        if $\theta_m^{in} < \frac{\pi}{2} - \alpha_m$ **then**
            Configuration A →B or C
            Calculate $A_{b,m}$ from Eq. (A.2) and $A_{c,m}$ from Eq. (A.5)
            Update θ_m from Eq. (13)
        end if
        Calculate $S_\alpha, \overline{\chi} = \frac{1}{\mathcal{T}} \int_0^t (1 - S_w) d\tau$, and $k_{r\alpha}$ from Eq. (8)
    end if
    Increase ΔP
end While

Imbibition displacement: Set the minimum entry pressure, P_{cap}^{min}

    Calculate $P_{cap,m}$ from Eq. (12) fro each tube m
    if $\Delta P < P_{cap,m}$ **then**
    Imbibe the respective tubes until static flow conditions are reached
    Estimate t from Eq. (10) and update χ_m from Eq. (15)
if $\theta_m < \frac{\pi}{2} + \alpha_m$ **then**
Configuration B →D
Estimate the area $A_{b,m} = \frac{3R_m^2}{2\tan\alpha_m}$
else Configuration C →D or E
if Configuration C →D **then**
Estimate the area $A_{b,m} = \frac{3R_m^2}{2\tan\alpha_m}$
else if Configuration C →E **then**
Estimate $A_{b,m}, A_{c,m}$, and layer $= A_{c,m}(\pi - \theta_{a,m}) - A_{c,m}(\theta_{h,m}^1)$
end if
end if
Calculate $S_\alpha, \overline{\chi} = \frac{1}{\mathcal{T}} \int_0^t (1 - S_w) d\tau$, and $K_{r\alpha}$ from Eq. (8)
Update θ_m from Eq. (13)
end if
Decrease ΔP
end while

The algorithm is repeated by controlling the pressure drop ΔP to generate data over a reasonable time window for carrying out the dynamic model correlation discussed below. We reduce the ΔP increment in the last cycle by three orders of magnitude compared to the first cycles in order to prolong exposure time and achieve the final WA in fewer cycles. This arbitrary control is performed for the purposes of presentation, but is not strictly necessary. After each step, a relative permeability data point is calculated according to Equation (8) and then used

to correlate the dynamic relative permeability models when a complete set of data are obtained.

3. Simulation results

The two-phase flow simulation tool at the pore-scale is implemented in MATLAB. Each tube in the bundle is assigned a different radius R, with the radii drawn from a truncated two-parameter Weibull distribution (Hui and Blunt, 2000):

$$R = (R_{\max} - R_{\min})\{ -\delta \ln[y(1 - \exp(-1/\delta)) + \exp(-1/\delta)]\}^{1/\gamma} + R_{\min}, \quad (16)$$

where $R_{\max}$ and $R_{\min}$ are the pore radii of the largest and smallest pore sizes respectively, and δ and γ are dimensionless parameters, and $y \in (0, 1)$ is a random variable. The rock parameters and fluid properties are listed in Table 1.

These parameters are coupled to the bundle-of-tubes model to simulate fluid conductance and relative permeability curves. In the following section, we present and discuss the simulated relative permeability and related results.

3.1. Initial and final wetting-state relative permeability

In section 2, we point out that end wetting state relative permeabilities are the foundation to characterize the dynamic relative permeability curves. Thus, it is natural to examine the end-state $k_{r\alpha}$-S_α relations before quantifying the dynamic relative permeabilities using the same pore-size distribution and fluid properties in Table 1. Thus, static $k_{r\alpha}$-S_α data is simulated by fixing the wettability at pre-specified initial θ_m^{in} and final θ_m^f values in each tube, see Table 1.

The simulated data and correlated models are shown in Fig. 3, where we compare the correlation for both the BC (in Eqs. (5) and (6)) and LET (in Eq. (7)) models.

The fitted parameters for the correlation models are found in Table 2.

Both the BC and LET correlations give an excellent match to the static relative permeability data.

As a complement, we tested the sensitivity of the static correlations (not shown here) for different pore-size distributions. For a simple bundle of capillary tubes, we find that the parameters L_n and T_w in the LET model are unity for any pore-size distribution. Furthermore, we observe in Table 2 that E_α are the only two parameters that change with a change in wettability, whereas all BC model parameters are sensitive to wettability change. There are other important features of the static LET correlations that are noteworthy. For instance, we can represent parameters L_w and T_n with a single parameter, which we denote λ. In addition, the parameter E_n is the inverse of E_w.

Taken together, the parameter space of the LET model can be reduced significantly to a two-parameter *reduced LET* model for each phase:

$$k_{rw} = E_n S_w^\lambda (E_n S_w^\lambda + 1 - S_w)^{-1}, \quad k_{rn} = (1 - S_w)(1 - S_w + E_n S_w^\lambda)^{-1}. \quad (17)$$

The model in Eq. (17) can be further reduced to a one-parameter model if we set λ to be constant (λ = 1.3) and allow E_n to be correlated according to the wetting condition.

We emphasize that the reduction in parameter space for the LET

model is limited to simple pore geometries, and in general the full LET model is necessary to describe relative permeability in real porous media systems.

3.2. Simulated relative permeability data

We simulate relative permeability for five drainage-imbibition cycles (see Fig. 4), while the tubes in the bundle are altered through time following the CA model (13). These data are generated with a pore-scale parameter $C = 10 \times 10^{-5}$, and the evolution in CA is shown in (see Fig. 5). Note that the CA change may be halted (temporarily) in the pores if the displacement is to configuration D after imbibition. In this case, the drainage curve may follow the previous imbibition path. However, the imbibition curve may show a deviation from the previous drainage curve if wettability is altered sufficiently.

According to the CA distribution in Fig. 5 and $k_{r\alpha}$-S_α curves in Fig. 4, a change in wettability from strongly to weakly water-wet does not affect relative permeability in any significant way. In other words, the first drainage relative permeability curve overlaps with the initial wetting-state relative permeability curve even though the CA has been altered from 0° to 60°. This result is in accordance with previous work for a pore-network model with a wettability range of $\theta_m = 0$° to 45° (Ahmed and Patzek, 2003). This negligible WA impact on $k_{r\alpha}$-S_α is in contrast to the capillary pressure–saturation relation, where a small change of CA impacts the P_c-S_α ath significantly (Kassa et al., 2020). However, imbibition/drainage displacement may not necessarily occur in monotonically increasing/decreasing order of pore-sizes when the wettability of the pores (some) are altered to intermediate/weakly hydrophobic. This results in a relative permeability–saturation path deviation as observed in Fig. 4.

For subsequent drainage-imbibition cycles, we observe that the wetting and non-wetting phase relative permeabilities steadily increase and decrease, respectively (see Fig. 4). This result corresponds to wettability evolving from hydrophilic to hydrophobic conditions (Fig. 5). This occurs because the original wetting phase prefers the larger pores as wettability shifts, while the originally non-wetting fluid prefers the smaller pores. As a consequence, relatively permeability is reduced for the non-wetting, while the wetting phase relative permeability is improved as the final wetting state is approached. Additional drainage-imbibition cycles would follow along the static curve for the final wetting state once the final CA (θ^f) is reached.

Analogous to the capillary pressure–saturation relation (Kassa et al., 2020), Fig. 4 shows long-term WA introduces dynamic hysteresis in the $k_{r\alpha}$-S_α relations for a bundle-of-tubes model. The $k_{r\alpha}$-S_α hysteresis imposes a non-unique relation between the relative permeabilities and saturation. This is one of the challenging features of WA during the quantification of the dynamics in relative permeabilities. To eliminate the hysteresis observed in the $k_{r\alpha}$-S_α relation, we projected the simulated relative permeability data onto the temporal domain $\overline{\chi}$ in Fig. 6. The temporal domain, $\overline{\chi}$ is the measure of the exposure history in averaged sense which defined as:

$$\overline{\chi} = \frac{1}{\mathcal{T}} \int_0^t (1 - S_w) d\tau. \quad (18)$$

Unlike $k_{r\alpha}$-S_α, $k_{r\alpha}$-$\overline{\chi}$ is uniquely related but non-monotonically i.e., it raises to one and decreases to zero in time along each drainage-imbibition cycle.

The WA process also affects the corner fluid distribution in each drainage-imbibition cycle. Fig. 7 shows the evolution of volume-averaged corner saturation for the wetting and non-wetting phases. The wetting-phase corner saturation decreases through time while the layer saturation grows. This is because wettability is altered from water-wet to hydrophobic and thus, the originally non-wetting fluid prefers to be in the corners. However, when pores become more hydrophobic, the corner water increases and bulges-out during imbibition. This process may result in a layer collapse in the fifth imbibition, where the layer
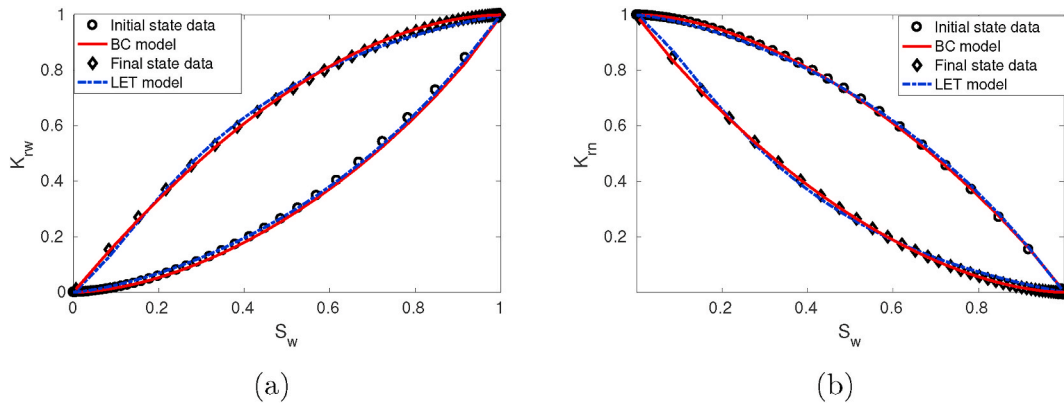
Table 1
Parameters used to simulate quasi-static fluid displacement in a bundle-of-tubes.

Parameter	value	unit	Parameter	value	unit
σ	0.0072	N/m	no. radii	500	[-]
$R_{\min}$	1	μm	$R_{\max}$	100	μm
θ_m^f	180	degree	θ_m^{in}	0.0	degree
μ_w	0.0015	Pa·s	μ_{nw}	0.0015	Pa·s
L	0.001	m	γ	0.5	[-]
δ	1.5	[-]			

Fig. 3. The BC and LET correlation models compared to the initial and final wetting-state relative permeability curves: (a) wetting phase and (b) non-wetting phase relative permeabilities.

Table 2
Estimated correlation parameter values for initial and final wetting-state relative permeability curves.

Model	Parameters	Initial CA (θ^{in})	Final CA (θ^f)
BC	a_w	0.9	1.839
	m_w	0.7329	0
	a_n	1.65	0.908
	m_n	0.075	0.7329
LET	L_w	1.3	1.3
	E_w	2.08	0.3
	T_w	1	1
	L_n	1	1
	E_n	0.48	3.37
	T_n	1.3	1.3

saturation increases as larger pores are imbibed and decreases when smaller pores are imbibed with increasing exposure time. Here, we have checked the establishment of corner fluids during the calculation of $k_{r\alpha}$-S_α relations in each drainage-imbibition displacements.

3.3. Dynamic relative permeability model correlation

3.3.1. Interpolation-based dynamic model

In previous work, we successfully applied the interpolation, i.e. Eq. (4), to capture time-dependent WA mechanisms in the capillary pressure

curves (Kassa et al., 2020). Thus, it is important to test the potential of the interpolation-based model to predict time-dependent dynamics in the $k_{r\alpha}$-S_α relation. The dynamic coefficient ω_α is calculated according to Eq. (2) and plotted in Fig. 8.

In Fig. 8b, we observe that the dynamic coefficient ω_α is related to the exposure time $\overline{\chi}$ non-monotonically. Thus, it is challenging to propose a functional relationship between ω_α and $\overline{\chi}$ directly. On the other hand, the dynamic coefficient ω_α in Fig. 8a is increasing with respect to the exposure time to the WA agent. However, the ω_α-S curves in Fig. 8a have piece-wise functional forms i.e., zero and Langmuir-type function of phase saturation, that are altered with exposure time. This imposes another challenge to find a smooth model to predict the curves along with the saturation. But, one can design a piece-wise function to correlate the $\omega_\alpha - S_\alpha$ data. From Fig. 8a, we observe that the starting point of the Langmuir functional form is exposure time-dependent along the saturation path. Thus, the $\omega_\alpha - S_\alpha$ can be represented as:

$$\omega_\alpha(S_w, \overline{\chi}) := \begin{cases} \dfrac{S_w - S_w^*(\overline{\chi})}{S_w - S_w^*(\overline{\chi}) + \beta(\overline{\chi})}, & \text{for } S_w > S_w^*(\overline{\chi}), \\ 0, & \text{otherwise} \end{cases} \quad (19)$$

where S_w^* and β are time-dependent. The variable S_w^* is used to transform the starting point of the Langmuir part ω_α along the saturation to zero, and β is used to determine the curvature of the curve. From Fig. 8a, we observe that the parameters S_w^* and β are decreasing functions of exposure time, $\overline{\chi}$.

We matched the designed model in Eq. (19) with the dynamic
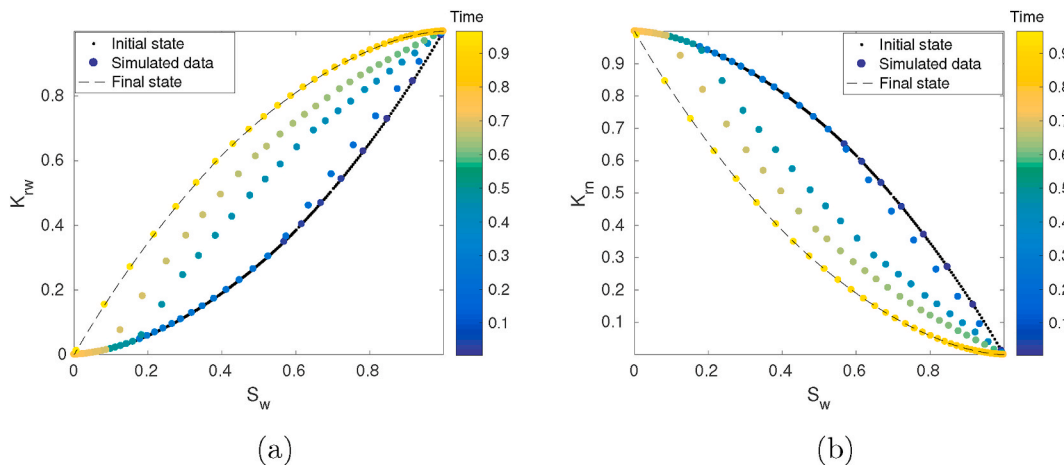

Fig. 4. Simulated dynamic relative permeability curves ((a) wetting phase and (b) non-wetting phase) with respect to wetting phase saturation. The static $k_{r\alpha}$-S_α curves for the initial and final wetting states are shown as a reference. The color code shows the $k_{r\alpha}$-S_α dynamics within a year of exposure time.
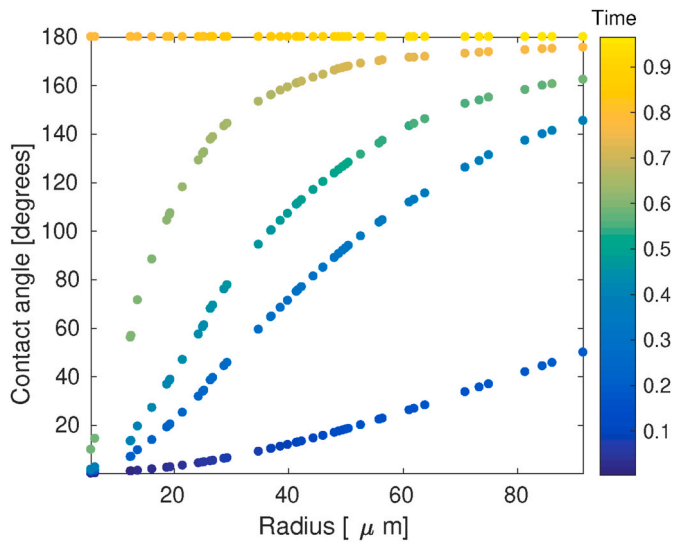
Fig. 5. Dynamic CA evolution as a function of exposure time to the WA agent per each tube. This CA distribution was recorded at the end of each drainage-imbibition cycle and the color code shows the CA dynamics during a year of exposure time.

coefficient data, $\omega_\alpha - S_w$, to describe the relations $S_w^* - \overline{\chi}$ and $\beta - \overline{\chi}$. The obtained relations have the form:

$$S_w^* = \zeta_1 \overline{\chi}^{b_1} + \psi_1, \text{and} \quad \beta = \zeta_2 \overline{\chi}^{b_2} + \psi_2, \tag{20}$$

where ζ_i, b_i and ψ_i for $i = 1, 2$ are dimensionless fitting parameters. These parameters are estimated and given in Table 3 for this particular simulation.

The models in Eqs. (19) and (20) are then substituted back into the interpolation model (4) to give the dynamic relative permeability model and is read as:

$$k_{r\alpha} = \begin{cases} \dfrac{S_w - S_w^*(\overline{\chi})}{S_w - S_w^*(\overline{\chi}) + \beta(\overline{\chi})} \left(k_{r\alpha}^f - k_{r\alpha}^{in}\right) + k_{r\alpha}^{in}, \text{ for } S_w > S_w^*(\overline{\chi}) \\ k_{r\alpha}^{in}, \quad \text{otherwise.} \end{cases} \tag{21}$$

The dynamic model (21) is compared with the simulated relative permeability in Fig. 9.

According to Fig. 9, the piece-wise interpolation model predicts beyond the initial wetting state at joint-point of the initial wetting-state model and the designed interpolation model. This shows that the designed model (21) is badly correlated with the simulated $k_{r\alpha}$-S_α data. Furthermore, the non-smoothness behavior of $\omega_\alpha - S_w$ results in a piece-wise phase relative permeability model with many dynamic parameters to be calibrated.

3.3.2. Parameter-based dynamic model

The second approach discussed in Section 2 relies on establishing a relation between the model parameters and $\overline{\chi}$ to upscale the effect of pore-scale wettability evolution in relative permeabilities. This is supported by the result reported in Table 2 for end wetting-state curves in which the model parameters are dependent on the wetting condition of the porous domain in addition to the pore-size distribution. As a consequence, we can formulate dynamic correlation models from
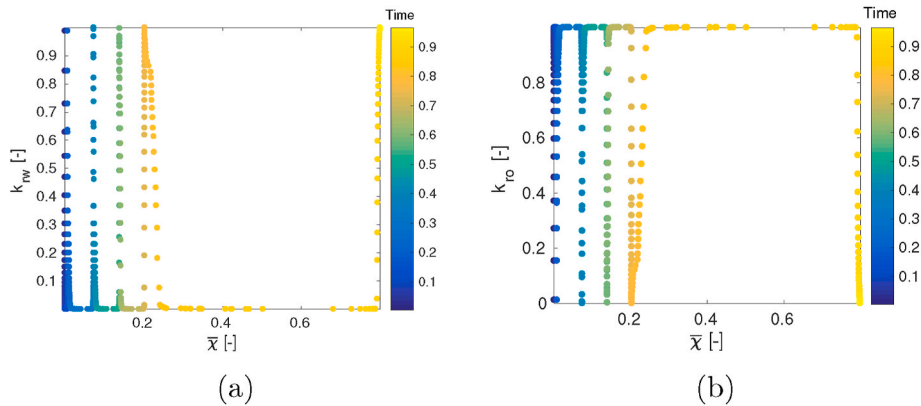

Fig. 6. Simulated relative permeability data as a function of $\overline{\chi}$ for (a) wetting phase, and (b) non-wetting phase. The color of each data point indicates the time elapsed in years.
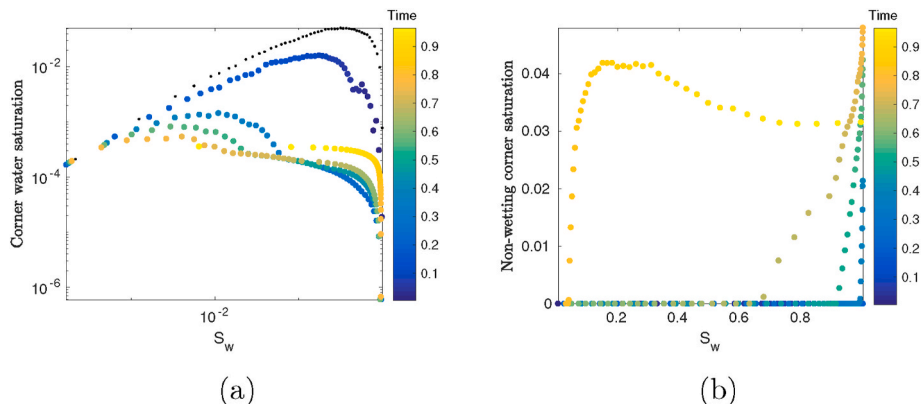

Fig. 7. Corner fluid saturations: (a) wetting phases saturation and (b) non-wetting phase saturation The color of each data point indicates the time elapsed in years.
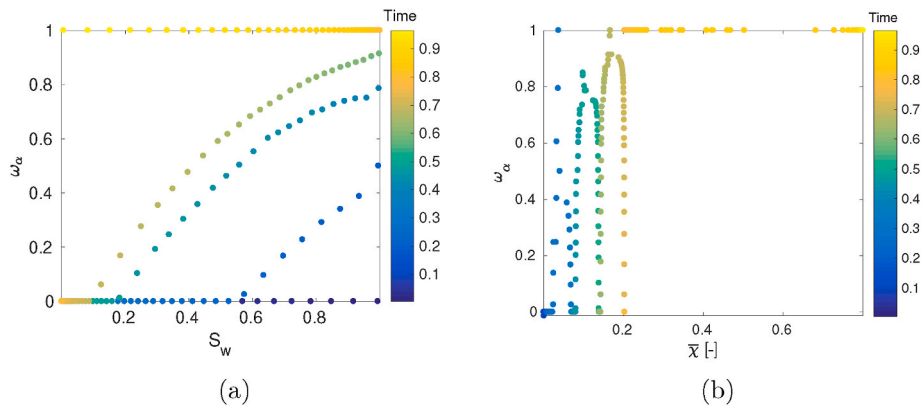
Fig. 8. The scaled dynamic deviation from the initial wetting-state relative permeability curves as a function of wetting phase saturation (a) and exposure time $\overline{\chi}$ (b).

Table 3
The estimated parameter values for the interpolation model.

Parameter	Value	Parameter	Value
ζ_1	0.0006123	ζ_2	0.001547
b_1	−2.522	b_2	−2.086
ψ_1	0.1297	ψ_2	0.2007

standard $k_{r\alpha}$-S_α relations, i.e., BC models in Eqs. (5) and (6) or reduced LET models in Eq. (17). So far, we noticed that only $E_n = 1/E_w$ is sensitive to wettability change in the reduced LET model, whereas both parameters are sensitive in the BC model (see Table 2). A model with fewer parameters is preferred in order to ease implementation in Darcy-scale flow models. Thus, we choose the reduced LET model when correlating to dynamic data using a parameter-based approach.

Based on these observations, we rearrange the reduced LET model:

$$k_{rw} = \frac{p\left(\overline{\chi}, E_n^{in}\right) S_w^\lambda}{p\left(\overline{\chi}, E_n^{in}\right) S_w^\lambda + 1 - S_w}, \text{and } k_{rn} = \frac{1 - S_w}{1 - S_w + p\left(\overline{\chi}, E_n^{in}\right) S_w^\lambda}, \tag{22}$$

where λ and E_n^{in} are determined from the initial wetting-state correlation. The reduced LET model (22) is then correlated to the $k_{r\alpha}$-S_α data in Fig. 4 with the curve-fitting tool in MATLAB and matched with the $k_{r\alpha}$-S_α data to study the functional dependencies between the p and $\overline{\chi}$. The obtained relation is linear and has the form:

$$p\left(\overline{\chi}, E_n^{in}\right) = \eta\overline{\chi} + E_n^{in}, \tag{23}$$

where E_n^{in} is as given in Table 2 and η is a *dynamic correlation parameter* for wetting and non-wetting phase relative permeabilities. For this particular simulation the dynamic parameter is estimated to be $\eta = 3.57$

for all drainage-imbibition cycles reported above. Now the dynamic term p in Eq. (23) can be substituted into the reduced LET model (22) to give the dynamic LET model:

$$k_{rw} = \frac{\left(\eta\overline{\chi} + E_n^{in}\right) S_w^\lambda}{1 - S_w + \left(\eta\overline{\chi} + E_n^{in}\right) S_w^\lambda}, \text{and } k_{rn} = \frac{1 - S_w}{1 - S_w + \left(\eta\overline{\chi} + E_n^{in}\right) S_w^\lambda}. \tag{24}$$

The correlated dynamic LET model in Eq. (24) and the simulated $k_{r\alpha}$-S_α data are compared in Fig. 10.

From Fig. 10, we observe that the proposed dynamic model (24) correlates well with the simulated relative permeability curves. The proposed dynamic relative permeability model is single-valued regardless of the number of drainage-imbibition cycles. However, this single-valued model is not well predictive around the junction points, particularly for low wetting-phase saturation. Despite this discrepancy, the obtained correlation result shown in Fig. 10 is acceptable and a significant improvement on the interpolation model result shown in Fig. 9. Furthermore, the dynamic LET model prediction can be improved by allowing λ to vary along the exposure time. However, this may double the number of parameters in the model that need to be calibrated.

If we compare the two dynamic models (i.e., the piece-wise interpolation model in Eq. (21) and the dynamic LET model in Eq. (24)), not only is the dynamic LET model a better fit to the data, it is easier to implement in a Darcy flow model than the piece-wise interpolation model. The reduced LET is likely more efficient to calculate because it is smooth in saturation-time space. We also note that the number of parameters in Eq. (24) is reduced by half from the original LET model. These all make the parameter-based dynamic model more reliable than using a model consisting of multiple parameters that change in each cycle (or hysteresis models). Further analysis below will concern only on the dynamic LET model.
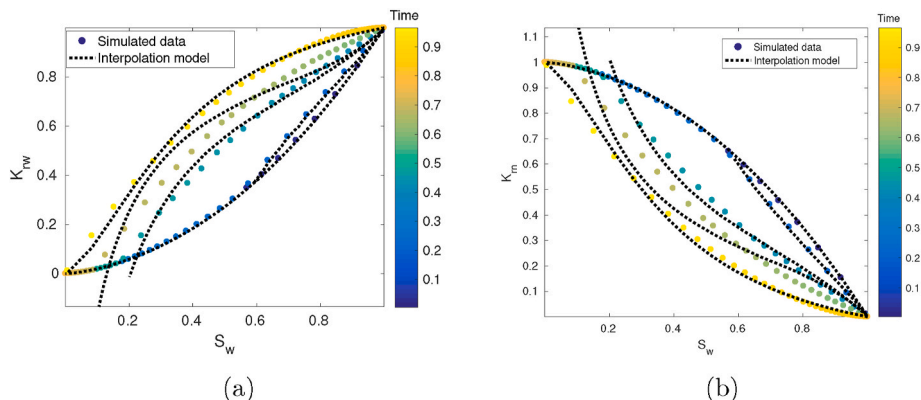

Fig. 9. Comparison of the interpolation model (21) with the simulated (wetting (a) and non-wetting (b)) relative permeabilities.
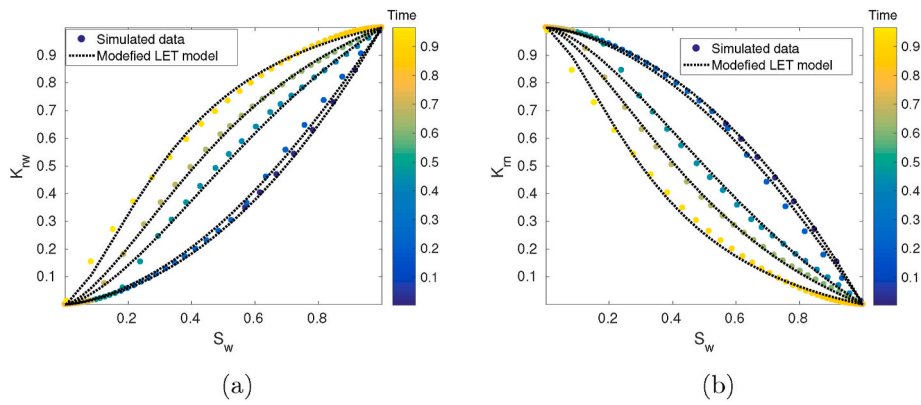
Fig. 10. Comparison of the dynamic LET model and the simulated phase relative permeability: (a) wetting phase and (b) non-wetting phase.

3.3.3. Sensitivity of correlated dynamic LET model to pore-scale WA

In this section, we will investigate the response of the upscaled model parameter η to the change in the CA model parameter C in Eq. (13). The parameter C controls the extent of WA at the pore-level, whereas η determines the WA induced dynamics in the relative permeabilities. We have simulated different drainage-imbibition $k_{r\alpha}$-S_α curves by varying C to draw a relation between η and C. To do so, we determine the parameter η from each $k_{r\alpha}$-S_α data that was simulated by considering different values of C. Then, we correlate the estimated parameter values of η with the chosen values of C, which can be read as:

$$\eta = \nu_1 C + \nu_2, \tag{25}$$

where ν_1 and ν_2 are fitting parameters. The correlation result is plotted in Fig. 11, where the parameters are estimated to be $\nu_1 = -1.8 \times 10^4$ and $\nu_2 = 6$. Therefore, we can predict the upscaled dynamics of the relative permeabilities directly from the pore-scale WA process.

The relation in Eq. (25) can be substituted into the dynamic relative permeability model (24) to complete the upscaling process. The resulting dynamic relative permeability models are saturation, exposure time, and pore-scale WA parameter dependent. The pore-scale parameter has to be estimated from the calibration of CA model (13) with experimental data. Validating the underlying CA change model is beyond the scope of this paper. Rather, we consider the CA model as a reasonable basis to perform and analyze the upscaling process.
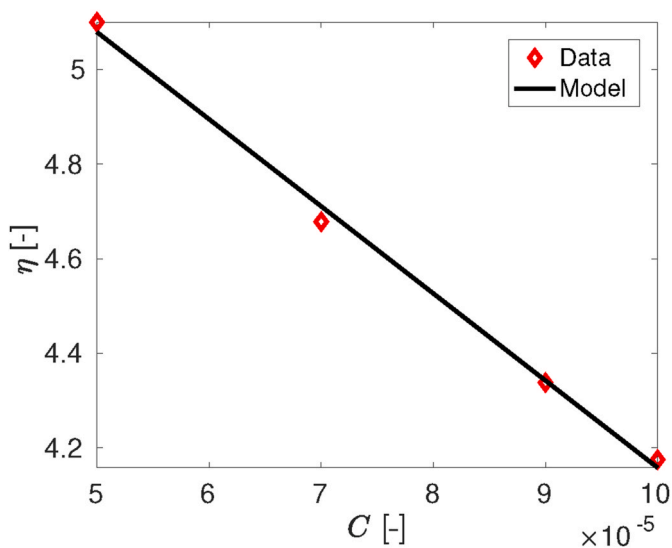
3.4. Applicability of the dynamic LET model to arbitrary saturation history

The path in saturation-time space used to generate the relative permeability data in Fig. 12 can be considered as one of many arbitrary paths in the domain $S_w \times \overline{\chi}$. The exact path is dependent on the history of the exposure time to the WA agent and the reversal-point of saturation. This implies that the relative permeability-saturation dynamics may behave differently if one chooses a different saturation path that entails a prolonged exposure time for a fixed saturation profile and/or flow reversal at intermediate saturation.

Here, we simulate a large number of possible $k_{r\alpha}$-S_α curves that involve different reversal-points and exposure history within the $S_w \times \overline{\chi}$. Note that we use the pore-scale model parameter $C = 10 \times 10^{-5}$. The simulated data is plotted in Fig.s. 12a and b for phase relative permeabilities. These arbitrary curves are used to test the robustness of the dynamic LET model in Eq. (24) by applying the model to generate the $k_{r\alpha}$-S_α-$\overline{\chi}$ surface and compare with the simulated data. The absolute difference between the simulated data and the surface generated by the calibrated model is depicted in Fig. 12c. According to the results in Fig. 12, we show that the dynamic LET model can be reliably applied to any saturation-time path having been calibrated against a single saturation history.

3.5. Discussion

In contrast to the dynamic capillary pressure model presented in Kassa et al. (2020), the interpolation-based approach is poorly correlated with the simulated relative permeability curves. However, further investigation (by considering advanced pore-network models) may be needed to re-evaluate the potential of capturing the WA process in the relative permeabilities based on the interpolation approach. We also examined the BC model in the parameter-based approach, though we do not report it here fully. For the sake of brevity, we have highlighted only the response of the BC model to the wettability change in Section 3.3 for end wetting conditions. In general, other models that involve more than two parameters (sensitive to CA change) could be calibrated with reasonable accuracy. But, these parameters need to be adjusted in each drainage-imbibition displacements. This complicates the modeling process and the resulting model may involve many parameters that may impose an extra challenge to analyze the WA impact on the flow dynamics at the Darcy scale.

In this study, we found that the original LET model with six total parameters (three for each phase) could be reduced to a dynamic LET model where only one parameter is needed to vary with wettability. The remaining parameters are only a function of pore-size distribution and the initial wetting state. The dynamic parameter $E_n = 1/E_w$ was then successfully correlated to the simulated dynamic relative permeability
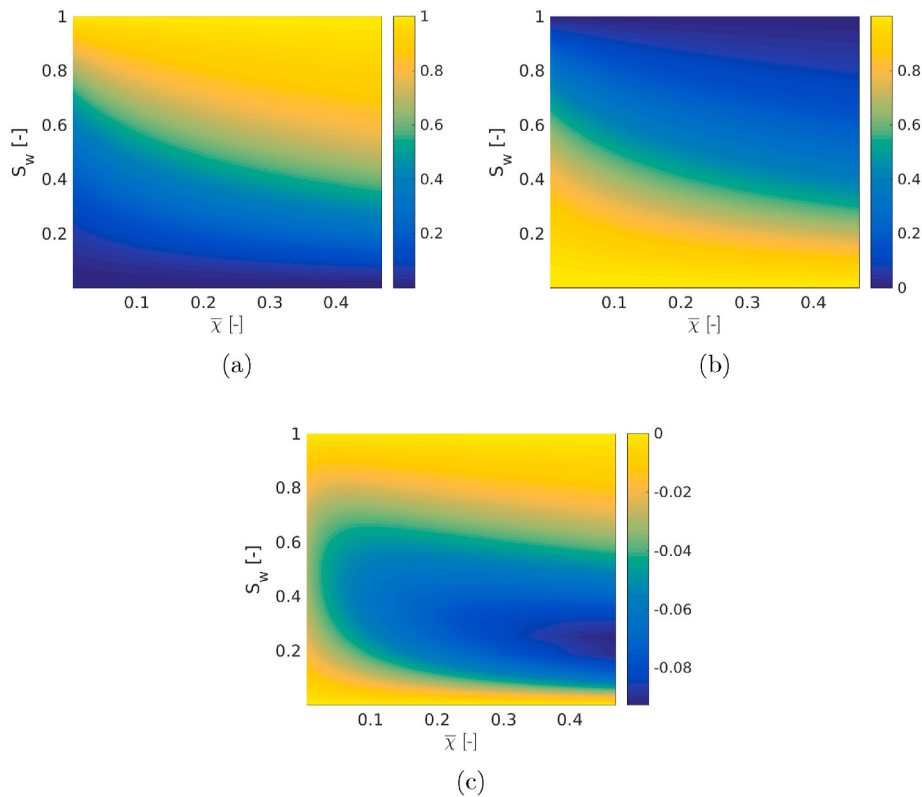

Fig. 11. The relation between pore-scale wettability parameter C and the correlation parameter η in Eq. (24).

Fig. 12. Top: Simulated relative permeabilities obtained by taking multiple paths in the $S_w \times \overline{\chi}$ space, for the wetting (left) and non-wetting (right) phases. Bottom: The difference between the dynamic model with the simulated data.

data. Furthermore, we found a clear relation between E_n and the exposure time $\overline{\chi}$ by introducing a dynamic parameter η. This approach results in a single-valued dynamic relative permeability model that represents any arbitrary exposure time history.

The dynamic LET model developed here may need to be extended for real porous media with connected pores and more complex geometry. For instance, mixed-wet media may exhibit *S*-shaped relative permeability curves, particularly for the non-wetting phase (Lomeland et al., 2005). In this case, it may be necessary to introduce additional dynamic parameters into the LET model proposed herein, i.e. L_w and T_n. Further investigation using more complex pore-scale models, e.g pore-network models, will be needed to generate the dynamic relative permeability data. We expect that the parameter-based approach using the LET model will still result in the best dynamic model even with more complex porous media. Further development of the dynamic LET model is the subject of future work.

The proposed model is at the Darcy scale, that allows for a change in relative permeability as a function of averaged variables such as saturation (S_w) and exposure time to a WA agent ($\overline{\chi}$). This implies that the relative permeability in a grid block that is exposed to the WA agent may change over time even for constant saturation profile. However, if the grid block is not exposed to the WA agent, $\overline{\chi}$ is zero for this particular grid block. In this case, the dynamic model predicts the initial wetting-state curve. However, the developed model may continue further after the end wetting-state curve has attained which is in contrast to the interpolation-type model, where prolonged exposure does not contribute to the dynamics once the final wetting curve is met, see (Kassa et al., 2020). Thus it is important to propose a strategy to ensure that the relative permeability dynamics do not to cross the end-state curve. From Eq. (23), we know that the final wetting state is attained when $\eta\overline{\chi} + E_n^{in} = E_n^{f}$ is satisfied. From this, we can estimate the exposure time needed to reach the final wetting state, $\overline{\chi}_{max} = \frac{E_n^{f} - E_n^{in}}{\eta}$, such that the relative permeability is represented by the end wetting-state curve. After

knowing this we can set the dynamic variable as

$$\overline{\chi} = \begin{cases} \frac{1}{\mathcal{T}} \int_{o}^{t} (1 - S_w) d\tau, & \text{if } \overline{\chi} < \overline{\chi}_{max} \\ \overline{\chi}_{max}, & \text{if } \overline{\chi} \geq \overline{\chi}_{max} \end{cases} \qquad (26)$$

This controls the unnecessary dynamics once the final wetting-state curve is predicted. Nevertheless, the dynamic term in the model pushes the relative permeability towards the higher and lower end of the curve for the wetting and non-wetting phases respectively.

Previous studies (Delshad et al., 2009; Yu et al., 2008; Anderson et al., 2015; Adibhatia et al., 2005) represent the impact of instantaneous WA on relative permeabilities by an interpolation model which can be matched to core-scale data in a heuristic manner. This study reveals that the interpolation model is not the best approach to upscale the pore-scale WA process. Rather, we have shown the potential of a dynamic LET model to capture the underlying WA process at the pore-scale. The proposed dynamic LET model is smooth and simple to use for practical applications. Most importantly, the model is designed to eliminate the hysteresis in relative permeability induced by CA change caused by exposure to a WA agent during drainage and/or imbibition displacements. Similar to the developments in Kassa et al. (2020), we have quantified the link between the pore-scale model parameter *C* and the core-scale parameter η. According to the simulation results, we have shown that a very simple scaling can relate a pore-scale process with the core-scale. This result implies that knowing the mechanism that determines the CA change at the pore-level can be used to predict the macroscale dynamics without performing pore-scale simulations. This is an important and valuable generalization for making use of experimental data to inform core-scale relative permeability-saturation relations.

4. Conclusion

In this paper, we developed a dynamic relative permeability model that includes the pore-scale underpinnings of WA in the relative permeability–saturation relationships at the Darcy scale. We found that the developed model (i.e., the modified LET model in Eq (22)) is simple to use and can predict WA induced changes in the relative permeabilities. The modified LET model shows a good agreement with the simulated relative permeability data. Furthermore, this model is independent of the saturation-time paths generated by any drainage-imbibition cycles. More importantly, the WA dynamics in the relative permeabilities is controlled by a single-valued parameter that has a clear relationship with the time-dependent CA change model parameter.

Credit author statement

Abay Molla Kassa: Conceptualization, Data curation, Writing - original draft, Writing - review & editing. Sarah E. Gasda: Conceptualization, Writing - review & editing. Kundan Kumar: Writing - review & editing. Florin A. Radu: Review & editing

Declaration of competing interest

The authors declare that they have no known competing financial interests or personal relationships that could have appeared to influence the work reported in this paper.

Acknowledgement

Appendix B. Supplementary data

Supplementary data to this article can be found online at https://doi.org/10.1016/j.petrol.2021.108556.

Nomenclature

Abbreviations

CO_2	Carbon dioxide
AMs	Arc meniscus
BC	Brooks-Corey
CA	Contact angle
Eq	Equation
Fig	Figure
LET	A model having parameters L, E, and T
MTM	Main terminal meniscus
WA	Wettability alteration

Superscripte

λ	Parameter in the reduced LET model
a, m	Fitting parameters in the Brooks-Corey model
b	The parameter in the interpolation model
dyn	Dynamic
f	Final wetting state
in	Initial wetting state
int	Fluid-fluid interface
k	Represents number of interface in the tube corner
L, T	Fitting parameters in the LET model
res	Reservoir

Subscripts

α	Phase indicator
max	Maximum
min	Minimum
b	Stands for bulk
c	Stands for corner
cap	Stands for capillary
h	Stands for hinging
i	The counter for the number of parameters
m	The m-th tube
n	Stands for nonwetting phase
p	Pore space
r, l	Stand for right and left respectively
s	Solid phase
T	Stands for total
w	Wetting phase

Liste of symbol

α	The half angle
β, ψ, ζ	b Fitting parameters in the interpolation model
$\chi, \overline{\chi}$	Pore-scale and averaged exposure time respectively
δ, γ	Parameters in the Weibull distribution
λ, E, η	Parameters in the modified LET model
$\mathscr{G}$	Conductance
K	Domain permeability
$\mathscr{T}$	Characteristic time
μ	Fluid viscosity
ω	The dynamic coefficient in the interpolation model
σ	Fluid-fluid interfacial tension
θ	Contact angle
φ	The dynamic term in the contact angle model
A	Cross-sectional area
C	CA model parameter
E	Fitting parameter in the LET model
f	Dynamic term in the relative permeability
k_r	Relative permeability
L	Tube length
P	Pressure
p	General parameter in the parametric approach
Q	Volumetric flux
q	Interface velocity
R	Radius of the inscribed circle
r	Radius of curvature
S	Saturation
V	Cross-sectional volume
x	The position along the tube length
y	Random variable

Appendix A. Calculations of areas covered by fluids

In Subsection 2.2, we showed the fluid configurations depending on the displacement scenario and wettability of the pore space. In this Appendix, we show how to calculate the areas that covered by the wetting and non-wetting phase fluids which demonstrated in Fig. 2. To do so, we numbered the fluid-fluid interfaces in order from the apex if there exist more than one interface in the corner, and we apply the indicator notation

$$I^k = \begin{cases} 1, & \text{if interface k separates bulk nonwetting and corner water} \\ -1, & \text{if interface k separates bulk water and corner nonwetting.} \end{cases} \quad (A.1)$$

The bulk cross-sectional area $A_{b,m}^k$ in each tube in the bundle is defined as,

$$A_{b,m}^k = \begin{cases} \dfrac{3R_m^2}{\tan \alpha_m} - 3r_m b_m^k \sin\left(\beta_m^k + \alpha_m\right) + 3r_m^2 \beta_m^k, & \text{if } I^k = 1, \\[4mm] \dfrac{3R_m^2}{\tan \alpha_m} - 3r_m b_m^k \sin\left(\beta_m^k - \alpha_m\right) - 3r_m^2 \beta_m^k, & \text{if } I^k = -1, \end{cases} \quad (A.2)$$

where

$$b_m^k = \frac{r \sin\left(\beta_m^k\right)}{\sin(\alpha_m)}, \text{ and } \beta_m^k = \begin{cases} \dfrac{\pi}{2} - \alpha_m - \theta_m^k & \text{if } I^k = 1 \\[3mm] \dfrac{\pi}{2} + \alpha_m - \theta_m^k & \text{if } I^k = -1. \end{cases} \quad (A.3)$$

Though we used a general notation for CA θ_m^k above, θ_m^k may be replaced by, $\theta_{r,m}$ and $\theta_{a,m}$ when the interface recedes and advances respectively, and $\theta_{h,m}^k$ if the interface, separating the bulk and corner fluids, is hinging. The hinging contact angle (if exists) changes with the entry pressure $P_{c,m}$ according to:

$$\theta_{h,m}^k = \begin{cases} \arccos\left(\dfrac{P_{c,m} b_m^k \sin(\alpha_m)}{\sigma}\right) - \alpha_m & \text{if } I^k = 1 \\[4mm] \arccos\left(\dfrac{P_{c,m} b_m^k \sin(\alpha_m)}{\sigma}\right) + \alpha_m & \text{if } I^k = -1. \end{cases} \quad (A.4)$$

The fluid area that occupies the corner regions can be estimated by

$$A_{c,m}\left(\theta_m\right) = 3r_m^2 \left(\theta_m + \alpha_m - \frac{\pi}{2} + \cos\left(\theta_m\right)\left(\frac{\cos(\theta_m)}{\tan(\alpha_m)} - \sin\left(\theta_m\right)\right)\right), \quad (A.5)$$

where θ_m is an argument to determine the appropriate area. The corner surface covered by water in configuration C is obtained by $A_{c,m}(\theta_{h,m}^1)$, whereas the non-wetting fluid layer in configuration E is calculated from $A_{c,m}(\pi - \theta_{a,m}) - A_{c,m}(\theta_{h,m}^1)$. The same approach can be applied if there exist many layers in the corner of the pore.

As clearly seen above the areas, $A_{b,m}$ and $A_{c,m}$ are dependent on wettability, i.e., fluid-fluid CA. For example, fluid configuration C and D occurs only if the condition $\theta_m \leq \frac{\pi}{2} - \alpha_m$ is satisfied during the drainage displacement (Helland and Skjæveland, 2006a). Otherwise, the non-wetting phase will completely displace the wetting from the tube, including the corners, and occupy the entire cross sectional area of the tube. In this case, the entry pressure calculation is reduced to the well known Young-Laplace equation. On the other hand, the non-wetting fluid layer occurs in the corner when the condition $\theta_m > \frac{\pi}{2} + \alpha_m$ is satisfied. This implies that a dynamic change of CA can also determine the fluid distribution in a single pore.

References

Adibhatia, B., Sun, X., Mohanty, K., 2005. Numerical studies of oil production from initially oil-wet fracture blocks by surfactant brine imbibition. In: SPE International Improved Oil Recovery Conference in Asia. SPE J. https://doi.org/10.2118/97687-MS

Ahmed, A., Patzek, T.W., 2003. The impact of wettability alteration on two-phase flow characteristics of sandstones–a quasi-static description. Water Resour. Res. 39 (1–10), 0.1029/2002WR001366,-2003.

Anderson, P.Ø., Evje, S., Kleppe, H., Skjæveland, S.M., 2015. A model for wettability alteration in fractured reservoirs. SPE J. 20, 1261–1275. https://doi.org/10.2118/174555-PA.

Anderson, W., 1987. Wettability literature survey-part 5: the effects of wettability on relative permeability. J. Petrol. Technol. 39 (11), 1453–1468. https://doi.org/10.2118/16323-PA.

Al-Mutairi, S.M., Abu-Khamsin, S.A., Hossain, M.E., 2012. A novel approach to handle continuous wettability alteration during immiscible CO$_2$ loading process. In: Abu Dhabi International Petroleum Conference and Exhibition. SPE.

Anderson, W.G., 1986. Wettability literature survey–part 1: rock/oil/brine interactions and the effects of core handling on wettability. J. Petrol. Technol. 38 (10), 1125–1144. https://doi.org/10.2118/13932-PA.

Bikkina, P.K., 2011. Contact angle measurements of CO^2-water-quartz/calcite systems in the perspective of carbon sequestration. Int. J. Greenh. Gas Contr. 5 (5), 1259–1271. https://doi.org/10.1016/j.ijggc.2011.07.001.

Blunt, M.J., 1997. Pore level modeling of the effects of wettability. SPE J. 2, 494–510. https://doi.org/10.2118/54454-PA.

Blunt, M.J., 2001. Flow in porous media–pore-network models and multiphase flow. Curr. Opin. Colloid Interface Sci. 6 https://doi.org/10.1016/S1359-0294(01)00084-X, 197–207.

Blunt, M.J., 2017. Multiphase Flow in Permeable Media: A Pore-Scale Perspective. Cambridge university press.

Bobek, J.E., Mattax, C.C., Denekas, M.O., 1958. Reservoir rock wettability–its significance and evaluation. SPE 213, 155–160. https://doi.org/10.2118/895-G, 01.

Bonn, D., Eggers, J., Indekeu, J., Meunier, J., Rolley, E., 2009. Wetting and spreading. Rev. Mod. Phys. 81, 739–805. https://doi.org/10.1103/RevModPhys.81.739.

Bradford, S.A., Leij, F.J., 1997. Estimating interfacial areas for multi-fluid soil systems. J. Contam. Hydrol. 27, 83–105. https://doi.org/10.1016/S0169-7722(96)00048-4.

Brooks, R.H., Corey, A.T., 1964. Hydraulic properties of porous media and their relation to drainage design. Trans. ASAE 7 (1), 26–28.

Buckley, J.S., Liu, Y., Monsterleet, S., 1988. Mechanisms of wetting alteration by crude oils. SPE J. 3, 54–61. https://doi.org/10.2118/37230-PA, 01.

Davis, A.N., Morton III, S.A., Counce, R.M., DePaoli, D.W., Hu, M.Z.-C., 2003. Ionic strength effects on hexadecane contact angles on a gold-coated glass surface in ionic surfactant solutions. Colloids Surf., A 221, 69–80. https://doi.org/10.1016/S0927-7757(03)00132-8.

Delshad, M., Lenhard, R.J., Oostrom, M., Pope, G.A., 2003. A mixed-wet hysteretic relative permeability and capillary pressure model for reservoir simulations. SPE Reservoir Eval. Eng. 6, 328–334. https://doi.org/10.2118/86916-PA.

Delshad, M., Najafabadi, N.F., Anderson, G.A., Pope, G.A., Sepehrnoori, K., 2009. Modeling wettability alteration by surfactants in naturally fractured reservoirs. SPE Reservoir Eval. Eng. 12 https://doi.org/10.2118/100081-PA.

Dickson, J.L., Gupta, G., Horozov, T.S., Binks, B.P., Johnston, K.P., 2006. Wetting phenomena at the CO$_2$/water/glass interface. Langmuir 22, 2161–2170. https://doi.org/10.1021/la0527238.

Du, Y., Xu, K., Mejia, L., Zhu, P., Balhoff, M., 2019. Microfluidic investigation of low-salinity effects during oil recovery: a no-clay and time-dependent mechanism. SPE J. 24, 2841–2858. https://doi.org/10.2118/197056-PA, 06.

Espinoza, D.N., Santamarina, J.C., 2010. Water-CO$_2$-mineral systems: interfacial tension, contact angle, and diffusion – implications to CO$_2$ geological storage. Water Resour. Res. 46, 1–10. https://doi.org/10.1029/2009WR008634.

Falode, O., Manuel, E., 2014. Wettability effects on capillary pressure, relative permeability, and irreducible saturation using porous plate. J. Pet. Eng. 1–12. https://doi.org/10.1155/2014/465418, 2014.

Farokhpoor, R.B., Bjørkvik, J.A., Lindeberg, E., Torsæter, O., 2013. Wettability behaviour of CO^2 at storage conditions. Int. J. Greenh. Gas Contr. 12, 18–25. https://doi.org/10.1016/j.ijggc.2012.11.003.

Haagh, M.E.J., Siretanu, I., Duits, M.H.G., Mugele, F., 2017. Salinity-dependent contact angle alteration in oil/brine/silicate systems: the critical role of divalent cations. Langmuir 33, 3349–3357. https://doi.org/10.1021/acs.langmuir.6b04470.

Helland, J.O., Skjæveland, S.M., 2006a. Three-phase mixed-wet capillary pressure curves from a bundle of triangular tubes model. J. Petrol. Sci. Eng. 52, 100–130. https://doi.org/10.1016/j.petrol.2006.03.018.

Helland, J.O., Skjæveland, S.M., 2006b. Physically based capillary pressure correlation for mixed-wet reservoirs from a bundle-of-tubes model. SPE J. 11, 171–180. https://doi.org/10.2118/89428-PA, 02.

Helland, J.O., Skjæveland, S.M., 2007. Relationship between capillary pressure, saturation, and interfacial area from a model of mixed-wet triangular tubes. Water Resour. Res. 43, 1–15. https://doi.org/10.1029/2006WR005698.

Hui, M., Blunt, M.J., 2000. Effects of wettability on three-phase flow in porous media. J. Phys. Chem. B 104, 3833–3845. https://doi.org/10.1021/jp9933222.

Iglauer, S., Paluszny, A., Pentland, C.H., Blunt, M.J., 2011. Residual CO$_2$ imaged with xray microtomography. Geophys. Res. Lett. 38, 1–6. https://doi.org/10.1029/2011GL049680.

Iglauer, S., Mathew, M., Bresme, F., 2012. Molecular dynamics computations of brine-CO$_2$ interfacial tensions and brine-CO$_2$-quartz contact angles and their effects on structural and residual trapping mechanisms in carbon geosequestration. J. Colloid Interface Sci. 386, 405–414. https://doi.org/10.1016/j.jcis.2012.06.052.

Iglauer, S., Pentland, C.H., Busch, A., 2014. CO$_2$ wettability of seal and reservoir rocks and the implications for carbon geo-sequestration. Water Resour. Res. 51, 729–774. https://doi.org/10.1002/2014WR015553.

Iglauer, S., Rahman, T., Sarmadivaleh, M., Al-Hinai, A., Fern, M.A., Lebedev, M., 2016. Influence of wettability on residual gas trapping and enhanced oil recovery in three-phase flow: a pore-scale analysis by use of microcomputed tomography. SPE J. 21, 1916–1929. https://doi.org/10.2118/179727-PA, 06.

Jadhunandan, P.P., Morrow, N.R., 1995. Effect of wettability on waterflood recovery for crude-oil/brine/rock systems. SPE Reservoir Eng. 10, 40–46. https://doi.org/10.2118/22597-PA.

Jafari, M., Jung, J., 2016. The change in contact angle at unsaturated CO$_2$-water conditions: implication on geological carbon dioxide sequestration. Geochem. Geophys. Geosyst. 17, 3969–3982. https://doi.org/10.1002/2016GC006510.

Jung, J.W., Wan, J., 2012. Supercritical CO$_2$ and ionic strength effects on wettability of silica surfaces: equilibrium contact angle measurements. Energy Fuels 26, 6053–6059. https://doi.org/10.1021/ef300913t.

Kassa, A.M., Gasda, S.E., Kumar, K., Radu, F.A., 2020. Impact of time-dependent wettability alteration on the dynamics of capillary pressure. Adv. Water Resour. 142 https://doi.org/10.1016/j.advwatres.2020.103631.

Kim, Y., Wan, J., Kneafsey, T.J., Tokunaga, T.K., 2012. Dewetting of silica surfaces upon reactions with supercritical CO$_2$ and brine: pore-scale studies in micromodels. Environ. Sci. Technol. 46, 4228–4235. https://doi.org/10.1021/es204096w.

Kjosavik, A., Ringen, J.K., Skjæveland, S.M., 2002. Relative permeability correlation for mixed-wet reservoirs. SPE J. 7, 49–58. https://doi.org/10.2118/77328-PA, 01.

Kovscek, A.R., Wong, H., Radke, C.J., 1993. A pore-level scenario for the development of mixed wettability in oil reservoirs. AIChE J. 39 https://doi.org/10.1002/aic.690390616, 1072–1085.

Landry, C.J., Karpyn, Z.T., Ayala, O., 2014. Relative permeability of homogenous-wet and mixed-wet porous media as determined by pore-scale lattice Boltzmann modeling. Water Resour. Res. 50, 3672–3689. https://doi.org/10.1002/2013WR015148.

Lashgari, H.R., Xu, Y., Sepehrnoori, K., 2016. Modelling dynamic wettability alteration effect based on contact angle. In: SPE Improved Oil Recovery Conference. SPE, pp. 1–17. https://doi.org/10.2118/179665-MS.

Li, K., Horne, R.N., 2006. Comparison of methods to calculate relative permeability from capillary pressure in consolidated water-wet porous media. Water Resour. Res. 42 (1–9).

Lomeland, F., Ebeltoft, E., Hammervold, T.W., 2005. A new versatile relative permeability correlation. In: International Symposium of the Society of Core Analysts. Society of Core Analysts.

Ma, S., Mason, G., Morrow, N.R., 1996. Effect of contact angle on drainage and imbibition in regular polygonal tubes. Colloid. Surface. 117, 273–291. https://doi.org/10.1016/0927-7757(96)03702-8.

Morrow, N.R., 1970. Physics and thermodynamics of capillary action in porous media. Ind. Eng. Chem. 62, 32–56. https://doi.org/10.1021/ie50726a006.

Morton III, S.A., Keffer, D.J., Counce, R.M., DePaoli, D.W., 2005. Behavior of oil droplets on an electrified solid metal surface immersed in ionic surfactant solutions. Langmuir 21, 1758–1765. https://doi.org/10.1021/la0480235.

Pentland, C.H., El-Maghraby, R., Iglauer, S., Blunt, M.J., 2011. Measurements of the capillary trapping of super-critical carbon dioxide in berea sandstone. Geophys. Res. Lett. 38 https://doi.org/10.1029/2011GL046683.

Plug, W.J., Bruining, J., 2007. Capillary pressure for the sand-CO$_2$-water system under various pressure conditions. application to CO$_2$ sequestration. Adv. Water Resour. 30 (11), 2339–2353. https://doi.org/10.1016/j.advwatres.2007.05.010.

Powers, S.E., Anckner, W.H., Seacord, T.F., 1996. Wettability of napl-contaminated sands. J. Environ. Eng. 122, 889–896.

Salathiel, R.A., 1973. Oil recovery by surface film drainage in mixed-wettability rocks. J. Petrol. Technol. 25, 1216–1224. https://doi.org/10.2118/4104-PA.

Saraji, S., Goual, L., Piri, M., Plancher, H., 2013. Wettability of scCO₂/water/quartz systems: simultaneous measurement of contact angle and interfacial tension at reservoir conditions. Langmuir 1–39. https://doi.org/10.1021/la3050863.

Sedaghat, M.H., Azizmohammadi, S., 2019. Dynamic wettability alteration in naturally fractured rocks. Comput. Geosci. 1–11. https://doi.org/10.1007/s10596-019-09843-6.

Spiteri, E.J., Juanes, R., Blunt, M.J., Orr, F.M., 2008. A new model of trapping and relative permeability hysteresis for all wettability characteristics. SPE J. 13, 277–288. https://doi.org/10.2118/96448-PA, 03.

Tokunaga, T.K., Jiamin, W., 2013. Capillary pressure and mineral wettability influences on reservoir CO_2 capacity. Rev. Mineral. Geochem. 77 (1), 481–503. https://doi.org/10.2138/rmg.2013.77.14.

Tokunaga, T.K., Wan, J., Jung, J., Kim, T.W., Kim, Y., Dong, W., 2013. Capillary pressure and saturation relations for supercritical CO_2 and brine in sand: high-pressure $p_c\ (s_w)$ controller/meter measurements and capillary scaling predictions. Water Resour. Res. 49, 4566–4579. https://doi.org/10.1021/acs.est.5b00826.

Treiber, L.E., Archer, D.L., Owens, W.W., 1972. A laboratory evaluation of the wettability of fifty oil-producing reservoirs. SPE J. 12, 531–540. https://doi.org/10.2118/3526-PA.

van Dijke, M.I.J., Sorbie, K.S., 2006. Existence of fluid layers in the corners of a capillary with non-uniform wettability. J. Colloid Interface Sci. 293, 455–463. https://doi.org/10.1016/j.jcis.2005.06.059, 02.

van Genuchten, M.T., 1980. A closed-form equation for predicting the hydraulic conductivity of unsaturated soils. Soil Sci. Soc. Am. J. 44, 892–898.

Vives, M., Chang, Y., Mohanty, K., 1999. Effect of wettability on adverse-mobility immiscible floods. SPE J. 4, 260–267, 03.

Wang, S., Tokunaga, T.K., 2015. Capillary pressuresaturation relations for supercritical CO_2 and brine in limestone/dolomite sands: implications for geologic carbon sequestration in carbonate reservoirs. Environ. Sci. Technol. 49, 72087217. https://doi.org/10.1021/acs.est.5b00826.

Wang, S., Edwards, I.M., Clarens, A.F., 2013. Wettability phenomena at the CO_2-brine-mineral interface: implications for geologic carbon sequestration. Environ. Sci. Technol. 47, 234–241. https://doi.org/10.1021/es301297z, 01.

Wang, S., Tokunaga, T.K., Wan, J., Dong, W., Kim, Y., 2016. Capillary pressure-saturation relations in quartz and carbonate sands: limitations for correlating capillary and wettability influences on air, oil, and supercritical CO_2 trapping. Water Resour. Res. 52, 6671–6690. https://doi.org/10.1002/2016WR018816.

Washburn, E., 1921. The dynamics of capillary flow. Phys. Rev. 7, 273–283.

Xu, W.S., Luo, P.Y., Sun, L., Lin, N., 2016. A prediction model of the capillary pressure j–function. PloS One 11, 1–9. https://doi.org/10.1371/journal.pone.0162123, 09.

Yang, D.D., Gu, Y.G., Tontiwachwuthikul, P., 2008. Wettability determination of the reservoir brine-reservoir rock system with dissolution of CO_2 at high pressures and elevated temperatures. Energy Fuels 22, 504–509. https://doi.org/10.1021/ef700383x, 01.

Yu, L., Kleppe, H., Kaarstad, T., veland, S. M. Skjæ, 2008. Modelling of wettability alteration processes in carbonate oil reservoirs. Netw. Heterogeneous Media 3, 149–183. https://doi.org/10.2118/174555-PA.